



**HAL**  
open science

## A broadband Ytterbium-doped tunable fiber laser for 3He optical pumping at 1083 nm

Geneviève Tastevin, Sébastien Grot, Emmanuel Courtade, Sylvain Bordais,  
Pierre-Jean Nacher

► **To cite this version:**

Geneviève Tastevin, Sébastien Grot, Emmanuel Courtade, Sylvain Bordais, Pierre-Jean Nacher. A broadband Ytterbium-doped tunable fiber laser for 3He optical pumping at 1083 nm. 2003. hal-00000608v2

**HAL Id: hal-00000608**

**<https://hal.science/hal-00000608v2>**

Preprint submitted on 25 Sep 2003 (v2), last revised 24 Feb 2004 (v3)

**HAL** is a multi-disciplinary open access archive for the deposit and dissemination of scientific research documents, whether they are published or not. The documents may come from teaching and research institutions in France or abroad, or from public or private research centers.

L'archive ouverte pluridisciplinaire **HAL**, est destinée au dépôt et à la diffusion de documents scientifiques de niveau recherche, publiés ou non, émanant des établissements d'enseignement et de recherche français ou étrangers, des laboratoires publics ou privés.

# A broadband Ytterbium-doped tunable fiber laser for $^3\text{He}$ optical pumping at 1083 nm

G. Tastevin<sup>1\*</sup>, S. Grot<sup>2</sup>, E. Courtade<sup>1,3</sup>, S. Bordais<sup>2</sup>, P.-J. Nacher<sup>1</sup>

<sup>1</sup> Laboratoire Kastler Brossel\*\*, 24 rue Lhomond, 75231 Paris cedex 05, France.

<sup>2</sup> Keospsys S.A., Department of Research and Development, 21 rue Louis de Broglie, 22300 Lannion, France.

<sup>3</sup> Present address : Dipartimento di Fisica, Università di Pisa, Via Buonarroti 2, I-56127 Pisa Italy.

September 25, 2003

**Abstract** Large amounts of hyperpolarized  $^3\text{He}$  gas with high nuclear polarization rates are required for use in neutron spin filters or nuclear magnetic resonance imaging of human lung. Very high efficiency can be obtained by metastability exchange optical pumping using multimode lasers to excite the  $2^3\text{S}$ - $2^3\text{P}$  transition at 1083 nm. Broadband Ytterbium-doped tunable fiber lasers have been designed for that particular application. Different options for the architecture of the fiber oscillator are presented and compared. Emphasis is given to a linear cavity configuration that includes a high reflectivity fiber mirror and a low reflectivity tunable fiber Bragg grating. Optical measurements are performed to finely characterize the spectral behavior of the lasers. Atomic response is also quantitatively probed to assess the optimal design of the oscillator for optical pumping. Multimode operation matching the 2 GHz Doppler-broadened helium resonance line and tunability over more than 200 GHz are demonstrated. Boosting the output of this fiber laser with a Yb-doped fiber power amplifier, all-fiber devices are built to provide robust, high power turn-key sources at 1083 nm for improved production of laser polarized  $^3\text{He}$ .

**PACS** 42.60.-v; 42.55.Wd; 32.80.Bx

## 1 Introduction

Laser-polarized  $^3\text{He}$  is used in a variety of research fields, ranging from low temperature to nuclear physics [1, 2, 3]. It has emerged in the past decade as a very promising tool for applications like the preparation of spin filters

for cold neutrons [2, 4], or magnetic resonance imaging of air spaces in human lungs [5, 6, 7]. This has strongly increased the demand for production of large amounts of gas with very high nuclear polarizations and high production rates. The most efficient method to meet both requirements is metastability exchange optical pumping (MEOP). It relies on optical pumping (OP) of the  $2^3\text{S}$  metastable state of helium with 1083 nm resonant light [8, 9]. Large nuclear polarizations can be prepared in a low pressure gas at room temperature within a few seconds [9, 10]. Polarization-preserving compression is performed after OP to obtain dense gas, with a choice of possible schemes depending on the targeted application [11, 12, 13]. Home-built 1083 nm light sources [1, 14] are now replaced by commercial lasers [10, 15, 16, 17]. Their development may lead to improved performances and open the way to a wider dissemination of this laser-based polarization technique.

For massive production of highly polarized  $^3\text{He}$  gas powerful amplifiers have been built, a progress due to the rapid development of fiber-based technology for telecommunications. They are operated in a conventional master oscillator power fiber amplifier configuration (MOPFA), with a seed laser providing the desired 1083 nm radiation (a DBR laser diode [16, 17] or a fiber laser [10]). OP rates are crucially determined by the number of atomic transitions induced per unit time, which depends both on the available power intensity and on the spectral characteristics of the laser emission. The laser cavity must hence be carefully optimized to efficiently match the spectral power distribution profile to the Doppler broadened atomic line.

The main objective of this article is to describe all-fiber 1083 nm laser oscillators specially designed for helium OP. To finely characterize their spectral characteristics and assess their performances a series of tests and measurements is performed. Absolute OP performances are actually difficult to determine because experimental results strongly depend on the choice of operating conditions. The second objective of this article is to present in

\* electronic mail : tastevin@lkb.ens.fr, Fax : 33-1-44323434

\*\* Research laboratory affiliated to the Université Pierre et Marie Curie and to the Ecole Normale Supérieure, associated to the Centre National de la Recherche Scientifique (UMR 8552)

detail the basic tests performed in order to provide reference tools that can be used to quantitatively characterize and appropriately compare all 1083 nm sources available for helium OP. Section 2 briefly compiles the relevant features of the  $2^3\text{S}$ - $2^3\text{P}$  transition and describes the currently used OP schemes to specify the main laser requirements. Section 3 describes the architecture of the fiber oscillators and the performed optical measurements. Section 4 focuses on the measurements of the atomic response to the laser spectral characteristics which provide a guide to optimal design of fiber lasers tailored to OP applications.

## 2 Metastability exchange optical pumping and laser requirements

MEOP is a polarization technique involving only helium atoms, based on an indirect spin orientation process [8, 9]. Due to hyperfine coupling in the  $2^3\text{S}$  state, OP on the electronic  $2^3\text{S}$ - $2^3\text{P}$  transition induces partial orientation of the nuclei of the metastable atoms. Metastability exchange occurs during collisions in which an incoming metastable atom transfers its electronic excitation energy to an incoming ground state atom, leaving the outgoing ground state atom with the partially polarized nucleus.

The structure of the low lying energy states of helium and of the  $2^3\text{S}$ - $2^3\text{P}$  transition at null magnetic field is indicated in Fig. 1. More details and numbers can

at room temperature. The Doppler full width half maximum (FWHM)  $D$  is on the order of 2 GHz for the helium atom (at 300 K  $D=1.98$  GHz FWHM for  $^3\text{He}$ , 1.72 GHz FWHM for  $^4\text{He}$ ).

MEOP is usually performed at low helium gas pressure (around 1 mbar) with a low applied magnetic field (up to a few mT). For OP of pure  $^3\text{He}$  one advantageously uses one of the two resolved components,  $C_8$  or  $C_9$  (respectively the  $2^3\text{S}$ ,  $F=1/2$  -  $2^3\text{P}_0$  and  $2^3\text{S}$ ,  $F=3/2$  -  $2^3\text{P}_0$  transitions) [9]. Isotopic mixtures may be efficiently pumped using the  $D_0$  line ( $2^3\text{S}$  -  $2^3\text{P}_0$  transition of  $^4\text{He}$ ) [15], significantly shifted from the  $^3\text{He}$  lines. To reach these three resonance lines the infrared pumping laser must be tunable over 40 GHz. The low applied magnetic field is required only to prevent fast magnetic relaxation and it has a negligible effect on the structure of the atomic states. In particular all Zeeman energy splittings are much smaller than the Doppler width and the pumping light must be circularly polarized to selectively depopulate adequate sublevels and deposit angular momentum into the gas. As nuclear polarization builds up the light absorption strongly decreases due to the depletion of the population in the pumped atomic sublevels. Simultaneously the absorption probability increases for light with the opposite circular polarization, so that any residual fraction of the pumping beam with that wrong circular polarization will very efficiently contribute to reduce the ultimate nuclear orientation [9,10]. In practice the beam polarization (and hence the optical quality of all elements along the light path including the OP cell windows) becomes especially crucial at high laser intensities. A set of high quality polarizing cube and low order quarterwave plate is usually inserted in front of the OP cell to get pure circular polarization. Therefore the laser light must have a linear polarization, whose long term stability directly determines that of the effective pumping power.

Operation at high magnetic field has recently been shown to yield improved OP performances at higher gas pressure [19,20]. The structure of the energy levels is strongly modified and the various Zeeman sublevels are no longer degenerate. This advantageously removes the stringent constraint on the degree of light polarization for the pumping beam. However it also substantially extends the required tunability range for the laser source, to nearly 150 GHz at 1.5 T for instance [18].

Extensive studies of the MEOP process have been performed in sealed glass cells over the past forty years. In order to populate the  $2^3\text{S}$  metastable state, a plasma discharge is sustained in the helium gas. In short, the steady state density of  $2^3\text{S}$  atoms (hence the OP light absorption and angular momentum deposition rates in the gas) increases with the plasma intensity. Yet various operating conditions (gas purity, pressure and cell dimensions) may set limits to the actual  $2^3\text{S}$  lifetime and density. The discharge also introduces substantial nuclear relaxation, due to collisions in the highly ex-

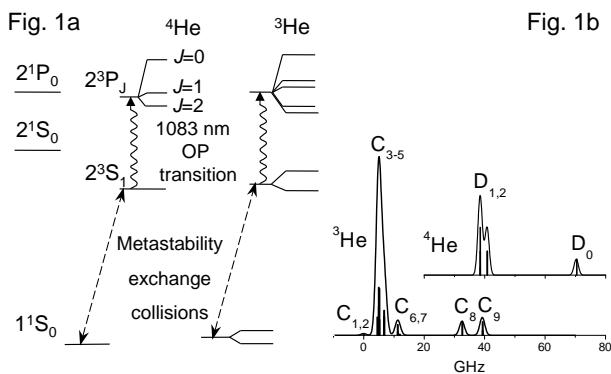


**Fig. 1** a: Low energy states of the He isotopes used for MEOP. b: Isotopic shift, fine and hyperfine structure of the  $2^3\text{S}$ - $2^3\text{P}$  transition lead to a 70 GHz frequency spread at null magnetic field.

be found in [18] and references therein. The atomic resonance lines are distributed over nearly 70 GHz, with line widths originating from various processes. The radiative decay rate of the  $2^3\text{P}$  state is  $1.02 \times 10^7 \text{ s}^{-1}$ . Atomic collisions introduce a pressure-dependent contribution ( $10^8 \text{ s}^{-1}/\text{mbar}$ ). For gas confined in an OP cell, the atomic lines are strongly Doppler broadened

cited states, emission of circularly polarized fluorescence light by the plasma [21], or formation of metastable  $\text{He}_2$  molecules at high pressures (a process enhanced at high laser powers due to massive promotion of He atoms to the  $2^3\text{P}$  state, where the cross section to produce these  $\text{He}_2$  molecules is 100 times larger than in the  $2^3\text{S}$  state [22]). The most favorable plasma conditions, which lead to highest polarizations but slow pumping rates, are usually found for weak discharges in a very pure He gas at low pressure for transverse cell dimensions of order a few centimeters. Indeed, the actual optimal plasma and pressure also depend on OP cell shape and size (e.g. due to radiation trapping), as well as on OP laser power and spectral characteristics [10].

The optimal operating conditions have recently been revisited due to the development of applications where large quantities of highly polarized  $^3\text{He}$  gas are needed. Most current schemes are based on gas flow through one or several OP cell(s), where it gets optically pumped at low pressure and mT magnetic field, and accumulation of compressed polarized gas in appropriate storage vessels [11,12,23]. Cell dimensions, materials and gas flow rates are optimized to achieve the best efficiency with the available laser source, which usually results from a trade off between high nuclear polarizations and fast production rates. In addition actual OP conditions may not be ideal (gas purity is for instance never as high as in carefully prepared sealed cells). Taking into account the finite transit time of the atoms in the OP cell, pressure, atomic transition line and discharge intensity are also often selected to shorten the OP time. In all cases the latter decreases at high photon fluxes, leading to improved performance when powerful lasers are available. The need for very high laser output powers is further increased by the rapid development of polarized  $^3\text{He}$  applications, which requires either to upscale the existing gas polarizers or to significantly improve the overall production rates in order to meet the growing demand for polarized gas.

MEOP is a very efficient and fast process. It typically yields 2 polarized nuclei per absorbed photon at 1083 nm, but this efficiency is reduced at high nuclear polarizations [10]. Therefore a strong increase in laser power is required to slightly improve the steady state nuclear polarization close to the limit set by the intrinsic non linear effects in OP [9].

To remain efficient at high laser powers and minimize line saturation effects, OP must involve the largest possible number of  $2^3\text{S}$  atoms, i.e. optimally interact simultaneously with all velocity classes. A singlemode laser is absorbed by atoms from a single velocity class, whose pressure-broadened line width  $\delta$  determines the fraction of  $2^3\text{S}$  atoms actually in resonance with the laser:  $X_s = \delta/D$  (typically 1 % at 1 mbar for pure  $^3\text{He}$  gas at room temperature). The photon absorption probability per atom (proportional to the power density, i.e. the light intensity per unit area) is equal to the spon-

aneous emission rate for a critical laser power density  $\mathcal{P}_{crit.} = 2\omega^3\hbar D X_s / 3\sqrt{\pi}c^2 T_{ij} = 0.277 X_s / T_{ij}$  ( $\text{W}/\text{cm}^2$ ), where  $\omega$  is  $2\pi$  times the resonance frequency,  $\hbar$   $1/2\pi$  times the Planck constant,  $c$  the velocity of light and  $T_{ij}$  the transition matrix element between the relevant atomic sublevels  $i$  and  $j$  [9]. It is of order  $10 \text{ mW}/\text{cm}^2$  for a circularly polarized singlemode laser ( $X_s=1\%$ ) tuned to the  $\text{C}_8$  line ( $T_{ij} = 0.29$ ), and  $1 \text{ W}/\text{cm}^2$  for a broadband laser emitting over the entire Doppler line width ( $X_s=1$ ). A more quantitative description of the impact of optical saturation on the OP dynamics can be derived from a realistic and detailed model of the OP process and from computer calculations taking into account the spectral and geometric features of the laser beam [10]. A single phenomenological parameter ( $X_s$ ) is used to specify the spectral coverage between the laser and Doppler profiles. This parameter is mainly determined by the laser line width and mode structure. Collisional redistribution between velocity classes also plays a role [18], but it is only crudely taken into account for the numerical simulations [10]. Attempts to accurately reproduce saturation profiles measured for narrowband laser sources bring out the need to improve such input parameters, and maybe also to include other effects like radiative broadening of resonance lines (at high laser powers) [24]. For a highly multimode laser, an optimal spectral coverage is expected to exist: on the one hand the number of atoms significantly excited by resonant light within the Doppler profile increases with the laser line width; on the other hand the laser efficiency decreases for an excessively broad emission spectrum, due to reduced absorption rates in the wings of the Doppler atomic line. Assuming for instance a continuous Gaussian laser frequency distribution of width  $L$ , the fraction of atoms submitted to more than half of the incident power varies as  $\text{erf}(\sqrt{Ln(2)}L/D)$ ; it starts growing almost linearly with  $L/D$  then rises more slowly, exceeding 90% for  $L/D > 1.4$ . In contrast the ratio of the total absorbed laser power to the incident one scales like  $1/\sqrt{1+L^2/D^2}$ ; it becomes for instance less than 50% for  $L/D > 1.7$ . Therefore the optimal coverage may be qualitatively inferred to lie around  $L \simeq D$ .

In summary, the OP rates basically depend on the number of atomic transitions induced per unit time, i.e. the light absorption rate, which in turn depends on the available power intensity but also on the spectral characteristics of the laser emission. Nevertheless a large number of operating conditions (pressure, cell dimensions, discharge intensity, gas purity, gas flow rate, etc.) play a role in the OP process, simultaneously and in an intricate way. It is thus very difficult to assess the efficiency of a particular laser source in terms of absolute OP performances. One way out may be the comparison of different types of laser sources under the same conditions [25]. But the variety of experimental parameters that need to be controlled and the difficulty encountered in obtaining identical beam divergences and intensity profiles for lasers require considerable effort. The choice of

operating conditions may also be critical, either to emphasize the relevant differences between the lasers or to test the sources in a configuration suited for a particular application. A different approach is presented in this article, which focuses on the laser spectral characteristics relevant for MEOP of  $^3\text{He}$ . The selected protocols provide conclusive results that hardly depend on the experimental conditions. Detailed information on the fiber laser line width and mode structure is obtained from purely optical measurements. Further characterization with very basic equipment is provided by tests of the atomic response on the  $2^3\text{S}$ - $2^3\text{P}$  transition at null nuclear polarization, which do not involve the intricate OP process.

### 3 Architecture and operation of the fiber lasers

#### 3.1 Tunable 1083 nm fiber lasers

Different laser sources have been used to optically pump  $^3\text{He}$  gas: DBR semiconductor lasers [15,26], arc lamp pumped Nd:LNA lasers [27]. Good results have been obtained with home-built multimode LNA lasers [1,14,28]. Wide dissemination and use outside the laboratory environment has however been hindered due to inherent drawbacks and difficulties: modest provision and commercial availability of high quality crystal rods, limited output power (5-8 W, due to severe thermal lensing effects inducing frequent rod breaking), low wall plug efficiency, need for routine cleaning and re-alignment of the open air laser cavity optics. The emergence of fiber technology has allowed the development of powerful light amplifiers (delivering tens of watts) and novel laser sources in the near infrared region. Fiber lasers involving an external cavity in Littrow configuration have recently been demonstrated to provide good efficiency and wide tunability range [29]. However, as explained in the previous section, narrowband emission sources are not well suited for OP purposes.

Powerful broadband all-fiber lasers are therefore developed for OP of  $^3\text{He}$ . They are based on the convenient MOPFA configuration. The master oscillator is a low power fiber laser designed for tunable, multimode emission at 1083 nm with a spectral range on the order of 1-2 GHz. A large output power is provided by a power booster, which can be separately optimized for maximal output efficiency. With adequate optical isolation between the two parts and operation of the power amplifier in the saturated regime, the spectral characteristics of the whole set-up are those of the master oscillator. Both the master oscillator (characterized in this work) and the power amplifier (described in detail in [30,31]) take advantage of the high gain provided by Ytterbium-doped double clad fibers (DCF) pumped by broad stripe laser diodes.

A comprehensive introduction to the capabilities of Yb-doped fiber lasers can be found for instance in [32].

The  $\text{Yb}^{3+}$  ion advantageously exhibits large absorption cross sections in the 915-925 nm range and a more important one around 975 nm, where low cost powerful laser diodes are commercially available for pumping. In a Ge co-doped silica matrix, transitions between sublevels of the ground  $^2\text{F}_{7/2}$  and excited  $^2\text{F}_{5/2}$  states result in two main emission lines: a narrow intense one at 975 nm and a broad one extending between 1 and 1.2  $\mu\text{m}$ . DCF are preferred for high power operation, the large inner cladding allowing propagation of the multimode pump beam around the doped active core and multiple crossing across it. Continuous wave (CW) operation with output powers exceeding 110 W has been demonstrated using DCF [33].

#### 3.2 The fiber oscillators

The architecture of the fiber laser oscillator is based on a Fabry-Pérot (FP) linear cavity closed by a high reflectivity fiber mirror and a tunable fiber Bragg grating (FBG). The gain section consists of a Yb-doped DCF pumped by a 975 nm laser diode (absorption: 0.9 dB/m) using the V-groove side pump technique (VSP<sup>®</sup>): the pumping light is launched through imbedded V-grooves formed directly into the DCF inner cladding and is totally reflected on the fiber side-wall, yielding up to 90% coupling efficiency [34]). The doped fiber length is about 3.5 m, it is not optimized in terms of output power and pump absorption in this work. Inside the protective polymer outer cladding, the inner glass cladding is about 200  $\mu\text{m}$  in diameter with a numerical aperture of 0.45 and a star shape profile to ensure efficient mode mixing and high absorption of the pump light in the doped area. A pair of all-glass silica fibers, single mode at 1  $\mu\text{m}$ , are spliced at both ends of the DCF to allow connection to the other fiber optical components.

The tunable FBG, used for frequency discrimination, serves as a low transmission output mirror for the laser cavity. The two key characteristics of the FBG are thus the FWHM of its operating range and the reflectivity. They both play an important role in setting the laser power and line width, and must be optimized and controlled. The tunable FBG is thermally isolated and temperature regulated to stabilize the laser frequency. Piezo-electrical control of mechanical strain applied to the grating allows fine tuning of the laser frequency to the helium resonance lines.

Fig. 2 displays the architecture of a fiber oscillator in which a loop mirror is used to close the FP linear cavity. Fiber loop reflectors are easily fabricated and exhibit large reflectivities (50-75%) over a broad frequency range [35]. The selective tunable FBG is spliced at the output end of the cavity. It directly controls both the operation frequency and the FWHM of the laser.

The operation of that loop mirror oscillator is hereafter fully characterized. Subsequent comparison is made

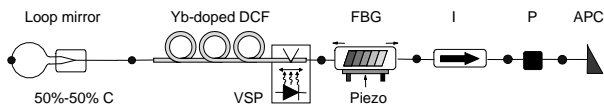


**Fig. 2** 1083 nm tunable broadband fiber oscillator. The linear laser cavity includes a fiber loop mirror formed by splicing the two ends of a 50%-50% coupler (C), a Yb-doped DCF and a selective FBG with piezo-control. An isolator (I) and a fiber polarizer (P) are fusion-spliced (solid dots) before the output angle polished connector (APC). V-groove side pumping (VSP) of the fiber is performed at 975 nm.

with another fiber oscillator based on the same FP linear cavity architecture, where the loop mirror is replaced by a high reflectivity FBG to fully optimize the laser for OP applications (see Fig. 12 in section 4, that depicts both this second oscillator and the power amplifier used to build the complete all-fiber MOPFA laser). The two fiber oscillators mainly differ by their temporal and spectral behavior.

### 3.3 Operation of the loop mirror oscillator

The optical spectrum of the loop mirror oscillator is shown in Fig. 3. The emission range of the oscillator duly

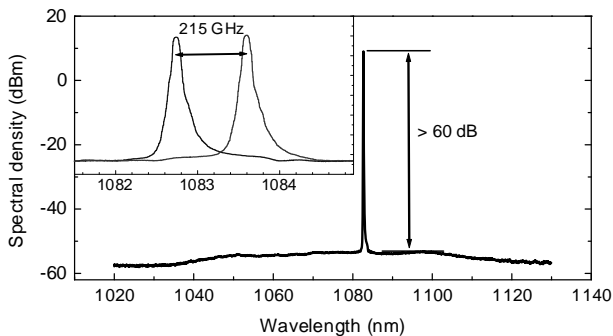


**Fig. 3** Optical spectrum of the loop mirror oscillator (resolution: 0.07 nm). Insert: fine tuning to the He lines is achieved by piezo-control of the selective FBG.

meets the laser requirements. It includes the whole  $^3\text{He}$  and  $^4\text{He}$  absorption spectrum (0.275 nm broad, starting at 1082.908 nm in air for  $D_0$  at null magnetic field). Piezo-control of the FBG actually allows fine tuning of the laser over 0.8 nm, i.e. more than 200 GHz (Fig. 3, insert). Therefore all components of the  $2^3\text{S}$ - $2^3\text{P}$  transition can be reached, even for OP in a 1.5 T applied magnetic field as indicated in section 2.

The loop mirror oscillator delivers up to 60 mW for a launched pump power  $P_{\text{pump}}=1900$  mW, with a laser threshold around  $P_{\text{pump}}=500$  mW (Fig. 4, open squares). A polarization-independent isolator protects the oscilla-

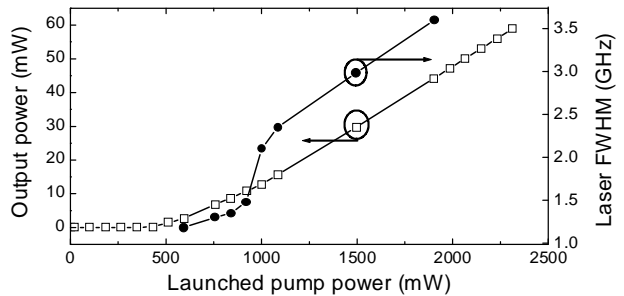


**Fig. 4** Output power (open squares, left vertical axis) and bandwidth (solid dots, right vertical axis) measured for the loop mirror oscillator. An abrupt FWHM increase occurs above  $P_{\text{pump}}=920$  mW.

tor from accidentally back-reflected light during operation. Linear polarization is achieved by a fiber polarizer spliced at the end of the laser cavity (extinction ratio  $>20$  dB). These two components induce a total 3 dB loss, taken into account to determine the power actually delivered at the output of the tunable FBG in Fig. 4.

The average spectral bandwidth (Fig. 4, solid dots) is measured using a FP analyzer (an air gap etalon whose cavity length is piezo-modulated at low frequency) with typically 10 GHz free spectral range (FSR) and 80 finesse. The laser modes are not resolved, the laser cavity FSR being in the MHz range. Substantial FWHM broadening is observed when the pump power is increased. An abrupt change in FWHM occurs above  $P_{\text{pump}}=920$  mW, in the absence of any correlated modification of the laser output power.

### 3.4 Temporal behavior and mode structure

Intensity noise (IN) measurements are performed for the loop mirror oscillator described in Fig. 2 using a photodiode with 700 MHz bandwidth connected both to a fast digital oscilloscope and to an electrical spectrum analyzer (ESA). Fig. 5 displays time variations of the output intensity and frequency spectra obtained at three pump powers ( $P_{\text{pump}} = 593, 839$  and 1167 mW). The frequency resolution (1 MHz) does not allow to characterize the frequency and repetition rate of the relaxation oscillations in the self-pulsing regime (see below and [30, 31, 37]). The peaks seen on the ESA output traces result from longitudinal modes emitted under the laser line width envelope beating together. This inter-modal beat signal gives access to the number and frequency splitting of the modes emitted on the probed time scale.

Three main types of behavior can be distinguished as the pump power is increased. The first one is observed near laser threshold (e.g. Fig. 5a:  $P_{\text{pump}}=593$  mW, laser FWHM 1.2 GHz). The laser operates spontaneously in self-pulsing regime, delivering series of pulses of sometimes relatively high peak power. This behavior is thus potentially harmful in view of subsequent high power

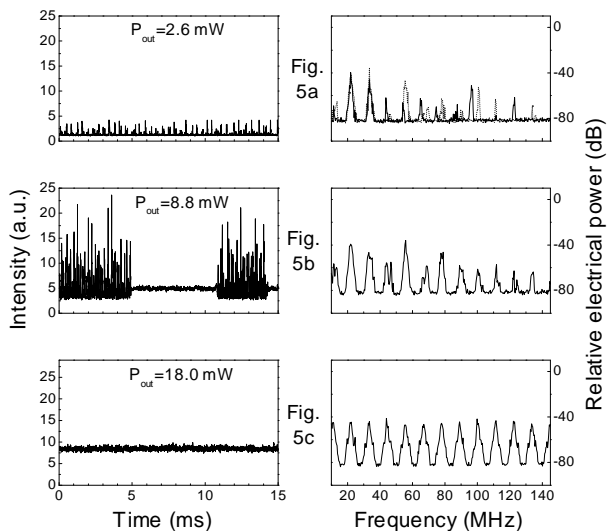


**Fig. 5** Time variations (left graphs) and frequency spectra (right graphs) of the laser intensity for the loop mirror oscillator. Fig. 5a:  $P_{\text{pump}} = 593$  mW; self-pulsing regime, with only a few emitted modes. The dotted line added in the right graph is a spectrum obtained from another randomly triggered singleshot recording (see text). Fig. 5b:  $P_{\text{pump}} = 839$  mW; unstable regime, switching between pulsed and CW operation. Fig. 5c:  $P_{\text{pump}} = 1167$  mW; stable regime, with CW and highly multimode operation. The output powers of the oscillator are indicated in the left graphs ( $P_{\text{out}}$ ).

amplification. The corresponding IN spectra only include beat frequencies below 150 MHz. Their statistical analysis shows that only peaks up to 40 MHz are always present, a few extra ones randomly appearing at frequencies that are other integer multiple of the FSR of the laser cavity. The second type of behavior (e.g. Fig. 5b:  $P_{\text{pump}} = 839$  mW, laser FWHM still below 1.5 GHz) is characterized by emission of intense light pulses alternating in time with CW light emission. In this case, inter-modal beat frequencies are regularly and permanently distributed under a typically 150 MHz wide envelope. The third and last type of behavior (e.g. Fig. 5c:  $P_{\text{pump}} = 1167$  mW and above) corresponds to a stable regime with a non zero power continuously emitted, even on atomic lifetime scale ( $0.1 \mu\text{s}$ ). A very large number of modes simultaneously exist inside the cavity: the IN spectrum is a comb of peaks with uniform frequency splitting (the cavity FSR) extending over the whole instrument limited detection bandwidth (the laser FWHM has jumped over the sharp discontinuity seen in Fig. 4 and is in that regime significantly larger than 2 GHz).

Strong non linear effects are known to occur in high gain rare-earth-doped fibers. The high powers supported by the Yb-doped DCF can lead to instabilities or huge intensity fluctuations due to distributed backscattering effects that are exacerbated in the linear cavity configuration [36,37]. Substantial variations of the laser bandwidth with pump power have been previously reported

[38], and intensity fluctuations as well as changes of the mode structure investigated [37], for Yb-doped fiber lasers in Littrow configuration. These dynamical behaviors are reminiscent of those obtained in Er-doped fiber lasers [39,40], but their exact physical origin in Yb-doped fibers may not be yet fully established [30,31,32,37]. Self-pulsing has been demonstrated to be dependent on passive cavity losses and favored at high losses [30,31,41]. The loop mirror used in the oscillator cavity has an intrinsic loss of order 1 dB and the reflectivity of the FBG is optimized. However significant losses may be due to technical difficulties encountered in achieving quality splices between the Yb-doped DCF and the pure silica fiber used for the junctions. Polarization dependent losses induced by the loop mirror are also expected to contribute to the occurrence of the self-pulsing regime. With the loop mirror oscillator, similar  $P_{\text{pump}}$  threshold values are observed for the changes of mode structure and temporal dynamics and for the variations of average FWHM. However the comparison of different types of linear cavity lasers indicates that it may well be fortuitous [30,31].

It is worth noting the correlation observed for this loop mirror oscillator between temporal behavior and mode structure: self-pulsing behavior and a limited number of emitted modes (Fig. 5a); stable intensity and multimode operation (Fig. 5c). In contrast, a different fiber oscillator based on a ring laser cavity (Fig. 6) exhibited stable output power but quasi-singlemode structure [24]. For that ring cavity laser (1.64 GHz FWHM) no ESA

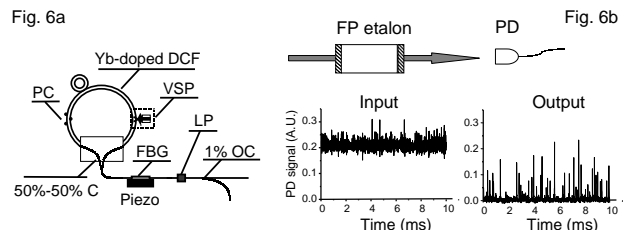


**Fig. 6** Fig. 6a: Ring cavity 1083 nm fiber oscillator (1.64 GHz FWHM) tested in [24]. PC: polarization controller, LP: linear polarizer, (O)C: (output) coupler. Fig. 6b, top part: Experimental set-up used for time resolved spectral analysis, including a FP etalon (1.5 GHz FSR, finesse: 100) and a fast photodiode (PD). Fig. 6b, bottom graph: Time variations of the input and output PD signal, respectively obtained without and with the FP etalon along the laser beam (solid arrow in Fig. 6b top part).

measurements had been performed. But on one hand the laser intensity had been monitored using a fast photodiode (response time well below  $1 \mu\text{s}$ ) and was indeed stable in time. On the other hand the light transmitted through a FP etalon with fixed length, FSR 1.5 GHz and spectral bandwidth 15 MHz (i.e. comparable to the  $2^3\text{S}$ - $2^3\text{P}$  radiative line width in the presence of collisions in a 1 mbar cell), was discontinuous. Non zero transmitted

intensities could be observed only for very short periods of time ( $6.7 \mu\text{s}$  on average, with  $0.2 \mu\text{s}$  rise time and  $0.2\text{-}0.5 \mu\text{s}$  fall time at  $1/e$ ), separated by long periods of null transmission ( $215 \mu\text{s}$  long on average). Assuming a large mode jitter over the observed 1.64 GHz FWHM to result in random coincidence of the modes frequencies with the transmission bandwidth of the FP etalon, statistical analysis of repeated measurements lead to the conclusion that only 3 or 4 laser modes were simultaneously emitted. This had been confirmed later by a low saturation threshold in light absorption measurements (method and meaning described in section 4) and explains the moderate OP performances of this ring laser despite its proper FWHM and CW operation [24].

Therefore the same FP filter is used with the loop mirror oscillator to perform similar tests, for comparison and cross-check with the ESA measurements. CW light is indeed transmitted above  $P_{\text{pump}} \simeq 1300 \text{ mW}$ , suggesting truly multimode laser operation on the relevant atomic time scale ( $0.1 \mu\text{s}$ ) in the stable regime. In contrast, in the self-pulsing regime light is seldom emitted in the FP spectral transmission bandwidth and the average durations of the null-transmission periods typically vary from 1 ms close to laser threshold, to 0.1 ms at  $P_{\text{pump}}=760 \text{ mW}$  for instance. These observations fully confirm the conclusions drawn from the above described IN measurements.

### 3.5 Mode dynamics

The comparison between the IN spectra and the measured FWHM of the loop mirror oscillator suggests that in the self-pulsing regime the measured broad laser bandwidth results from very large mode jitter inside the cavity. In order to confirm this and to directly observe the mode dynamics, we observe the time variation of the beat signal between the fiber oscillator output and that of a singlemode 1083 nm DBR diode (50 mW output power, 3 MHz bandwidth [15]). To conveniently tune the two lasers to one another to better than 1 GHz, a fluorescence signal from a sealed  $^3\text{He}$  cell is used.

Fig. 7b to 7d display power spectra obtained by fast Fourier transform of single shot digital recordings (duration:  $0.1 \mu\text{s}$ , 5 ms and 0.1 s respectively) of the signal delivered by a fast photodiode located on the path of the two superimposed beams. The DBR diode is operating at fixed frequency (typically a few hundred MHz away from the central frequency of the fiber oscillator) and the oscillator is used at low pump power ( $P_{\text{pump}} = 593 \text{ mW}$ , self-pulsing regime). For comparison a spectrum obtained without the DBR diode beam (recording time:  $0.1 \mu\text{s}$ ) is shown in Fig. 7a. The low frequency parts of the heterodyne IN spectra (DBR diode plus fiber oscillator) in Fig. 7b to 7d are identical to those obtained with the fiber oscillator alone (homodyne autocorrelation spectrum) using the same set-up (Fig. 7a) or using the ESA (see Fig. 5a). As detailed in the previous

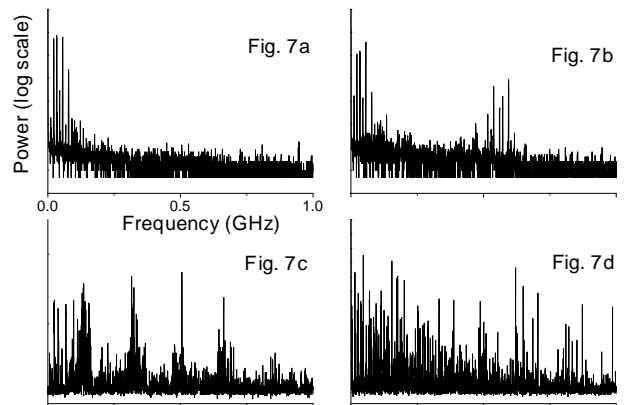


**Fig. 7** IN spectra of the loop mirror oscillator beam alone (Fig. 7a) or superimposed with that of a DBR diode (Fig. 7b to 7d), in the self-pulsing regime ( $P_{\text{pump}} = 593 \text{ mW}$ ). All plots have identical frequency span, 1 GHz full scale. Fig. 7a and 7b:  $0.1 \mu\text{s}$  recording time. The autocorrelation spectrum of the oscillator (Fig. 7a) also appears in Fig. 7b at low frequencies. The beat signal of the fiber laser and the singlemode diode (set of peaks around 0.6 GHz in Fig. 7b) indicates that only a few modes are simultaneously emitted. Mode jitter is evidenced by the broad spread of the beat peak frequencies as the recording time increases (Fig. 7c: 5 ms, Fig. 7d: 0.1 s).

subsection they correspond to the inter-modal beat signal of the fiber oscillator. At higher frequencies series of peaks appear which correspond to the beat signal of the diode and the oscillator. Frequency splittings are here again set by the fiber cavity FSR. Only one comb of beat peaks appears at very short recording times (Fig. 7b). Repeated measurements demonstrate that close to laser threshold a very small number of contiguous modes are indeed emitted on the atomic time scale ( $0.1 \mu\text{s}$ ). On one hand the central frequency of this comb of beat peaks is observed to change from shot to shot, randomly located within the detection bandwidth (of order 1 GHz). The frequency stability of the DBR diode is checked by the observation of the beat signal between two different DBR diodes in the same experimental conditions. The time variations of the beat frequencies are thus attributable to the oscillator only. On the other hand the spectra of single shot recordings taken on much longer time scales (several ms or more) display a continuous comb of beat peaks extending beyond 1 GHz (see Fig. 7d). Both observations confirm that a large jitter of a small number modes is responsible for the large average oscillator FWHM measured with the modulated FP etalon in the self-pulsing regime. They also indicate that for He atoms the laser would appear as quasi-singlemode despite this broad apparent optical spectrum.

Away from the laser threshold, the number of modes beating with the diode increases with the pump power. Broadband ( $\geq 1 \text{ GHz}$  FWHM) multimode operation on the atomic time scale is observed in the stable regime. However no further information can be obtained at high



$P_{pump}$  due to the limited detection bandwidth in this experiment.

Finally the observed temporal behavior, mode structure and dynamics are checked to remain totally unchanged when the output of the laser oscillator is launched into a saturated fiber power amplifier, as expected.

## 4 Atomic response to laser characteristics

### 4.1 Line width measurements

Unsophisticated but accurate measurements of the laser average FWHM can be achieved using a sample of  $^3\text{He}$  gas. The piezo control is used to sweep the oscillator frequency over the  $C_8$  and  $C_9$  lines. Fluorescence light (or laser absorption) at null nuclear polarization is monitored using a photodiode to extract the resonance line width for a weak probe beam intensity. Power densities well below a few  $\text{mW}/\text{cm}^2$  are needed to avoid saturation (see next subsection). When circularly polarized light is used a strong local field inhomogeneity must be imposed in the He cell to prevent nuclear polarization build-up, which would significantly alter the line profiles [18]. At high laser intensities finite orientation can still be produced in the metastable state despite strong nuclear relaxation in the ground state (over-polarization of the  $2^3\text{S}$  atoms [10]) and the best way to avoid OP effects is to use linearly polarized light. In any case the measured relative amplitudes of the two resonance peaks must correspond to the known ratio of the  $C_8$  and  $C_9$  line intensities (1.284 at very low magnetic field). Absolute calibration of the frequency scale is provided by the hyperfine splitting between  $C_8$  and  $C_9$  (6.74 GHz). The experimental resonance line width results from the convolution of the atomic Doppler profile with the spectral envelope of the laser.

Recorded signals are very well fit by a set of two Gaussians of FWHM  $D_{\text{exp}}$ , which indicates that the laser spectral profile is actually very close to Gaussian [30,31]. The laser FWHM  $L$  is thus given by  $L^2 = D_{\text{exp}}^2 - D^2$ . Fig. 8 displays the obtained laser FWHMs as a function of the pump power for the loop mirror oscillator. The measured variation is in good qualitative agreement with the behavior discussed in section 3 (little change up to  $P_{\text{pump}}=920$  mW, then abrupt broadening and linear increase above  $P_{\text{pump}}=1100$  mW). The noticeable quantitative difference (20-30%) between these FWHM results and those obtained with the FP analyzer (Fig. 4, solid dots) mainly arises from the fact that two measurements were not performed in the same frequency range. Indeed, over the 200 GHz broad tuning range, the operating conditions of the laser cavity vary due to changes in the loop mirror reflectivity [35]. The influence of the mirror characteristics on the laser FWHM is analyzed and discussed in more detail in [30,31]. Experimentally, using the piezo-modulated FP analyzer to monitor the

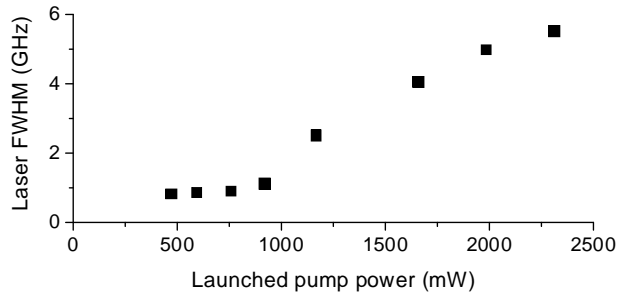


**Fig. 8** FWHM of the loop mirror oscillator obtained from  $C_8$  and  $C_9$  resonance linewidth measurements.

laser FWHM (see section 3), we actually observe changes of order 20% with operating frequency between the extreme limits of the tuning range of the loop mirror oscillator. The amplitudes of these FWHM changes depend on how close to threshold the laser is operated. Therefore for OP applications the laser should be kept working in stable operating conditions and precisely characterized at the atomic frequency used to polarize the gas.

### 4.2 Absorption measurements

Absorption measurements provide quantitative information on the actual fraction of light that can be used for efficient OP of the atomic nuclei. Laser absorption is measured as a function of the incident power density for the oscillator tuned to the  $C_9$  resonance line, in a sealed cell (5 cm long, 5 cm in diameter) filled with 1.6 mbar of ultrapure  $^3\text{He}$  gas. In order to perform accurate comparison between several operating conditions of the laser cavity measurements are performed successively with identical discharge conditions to keep the  $2^3\text{S}$  number density constant. The same basic equipment is required, except that a lock-in amplifier advantageously improves the signal-to-noise ratio at low laser powers. As the laser power is varied, care is taken to keep the photodiode operating at nearly constant output level (using attenuators) to avoid possible biases due to saturation or non-linear response of the device. The gas is also always maintained at null nuclear polarization. The laser beam with Gaussian transverse intensity profile is expanded and a diaphragm of known open area is inserted to select a small central fraction of the collimated beam. Over the probed section the radial variation of the laser power has been checked not to exceed a few percents, so that the (quasi)uniform power densities are precisely determined from absolute power measurements. To reach strong optical saturation of the gas sample and to complete the investigations close to laser threshold, a 0.5 W fiber amplifier is used to boost up the light power delivered by the laser oscillator.

The relative absorption data plotted in Fig. 9a correspond to absorption rates measured with the loop mirror oscillator for different values of the launched pump

power, normalized to the maximum absorption rate obtained at very low power intensities for each  $P_{\text{pump}}$ . At

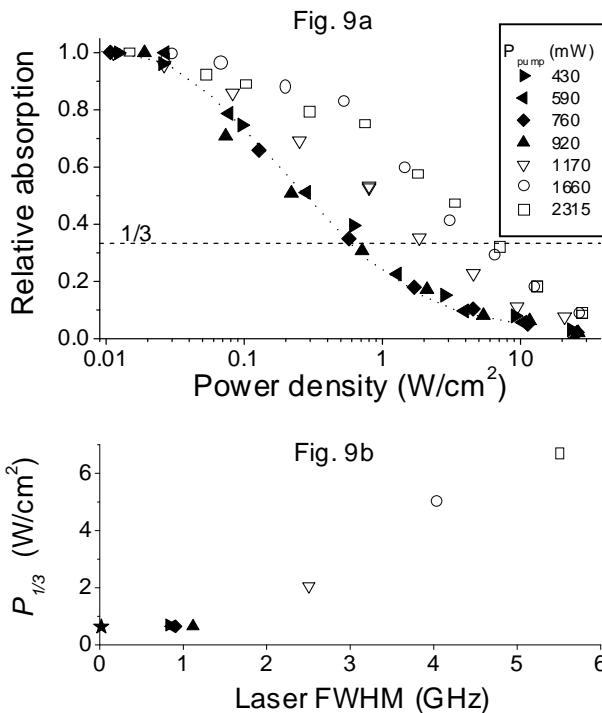


**Fig. 9** Fig. 9a: Relative absorption (see text) versus laser power density. Symbols: loop mirror oscillator operated at low (solid symbols) and high (open symbols) launched pump powers; 1.6 mbar  $^3\text{He}$  cell, light with circular polarization tuned on the  $\text{C}_9$  line. Dotted line: singlemode DBR diode, reference absorption profile from [24]; same cell, very similar experimental conditions. Fig. 9b: Saturation threshold  $\mathcal{P}_{1/3}$  (see text) versus laser FWHM. Solid and open symbols from Fig. 9a: loop mirror oscillator. Star: singlemode DBR diode.

low launched pump powers (solid symbols) the absorption profiles do not vary much with  $P_{\text{pump}}$ . They are quite similar to those usually obtained with a singlemode DBR diode (Fig. 9a, dotted line: data from reference [24], obtained in the same cell with comparable discharge conditions and measurement protocol). This confirms the conclusion drawn from the optical measurements and spectral analysis in section 3 for the unstable and self-pulsing regimes. As pump power is increased, the strong decrease of absorption due to optical saturation suddenly occurs at much higher power densities. This change in atomic response to laser excitation is a signature of the abrupt transition of the oscillator to the broadband multimode emission regime. At high launched pump powers (above  $P_{\text{pump}}=920$  mW, open symbols) the relative absorptions measured for a fixed power density become significantly larger when  $P_{\text{pump}}$  is increased

To characterize this change in behavior we introduce the power density  $\mathcal{P}_{1/3}$  where the measured ab-

sorption reaches 1/3 of its maximum value (dashed line in Fig. 9a).  $\mathcal{P}_{1/3}$  is plotted in Fig. 9b as a function of the loop mirror oscillator FWHM. It indeed remains almost constant up to  $P_{\text{pump}}=920$  mW, and close to the  $0.64 \text{ W}/\text{cm}^2$  value typically obtained with the singlemode diode (solid star, Fig. 9b). It then increases quite linearly with the laser FWHM above  $P_{\text{pump}}=1100$  mW. This sudden change of absorption saturation threshold correlates precisely with the abrupt change in spectral behavior described in section 3.

A relevant quantity for the OP process is the total number of absorbed photons per second, since it is the angular momentum deposition rate that determines the actual number of oriented nuclei. Absolute absorption rates are therefore plotted in Fig. 10 (same measurements performed with the loop mirror oscillator, data without normalization). At all light power densities the

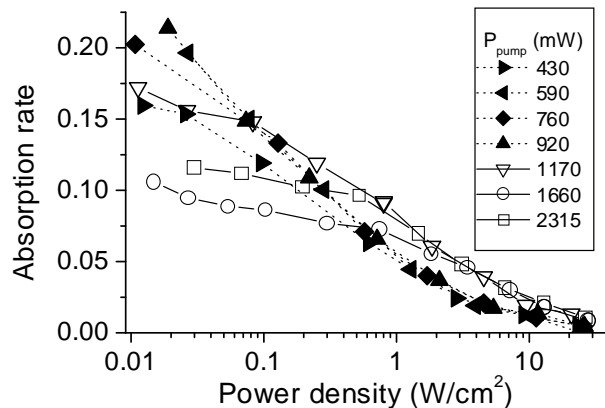


**Fig. 10** Absorption rates versus power densities for the loop mirror oscillator (same data sets as in Fig. 9, but without normalization to maximum values). The variations of absorption rates, hence of laser efficiency, with launched pump powers result from changes in the number of emitted laser modes (despite identical average FWHM, solid symbols) or from changes in the amount of off-resonance laser power (open symbols).

absorption rates are observed to vary by more than a factor 2 over the probed range of launched pump powers. For small  $P_{\text{pump}}$  (solid symbols) the absorption rates at low laser intensities rapidly vary with power density down to  $10 \text{ mW}/\text{cm}^2$ . They tend to increase with  $P_{\text{pump}}$ , as can be expected due to the increased number of emitted laser modes at resonance with the atoms. Differences however become hardly noticeable above a few hundreds  $\text{mW}/\text{cm}^2$ . For  $P_{\text{pump}} > 920$  mW (open symbols) saturation effects are small at very and moderately low power densities. The maximum absorption rates decrease when  $P_{\text{pump}}$  rises due to excessively large laser FWHMs (useless power emitted outside the Doppler line). At higher laser powers (above  $1 \text{ W}/\text{cm}^2$ ) the absorption rate is nearly twice larger than that obtained at low  $P_{\text{pump}}$  be-

cause of multimode light emission by the loop mirror oscillator. This absorption rate is observed to be independent of  $P_{\text{pump}}$ , which means that the measured change of relative absorption and saturation threshold (Fig. 9) is exactly compensated by the effect of strongly increased FWHMs in that regime (Fig. 8). Above  $20 \text{ W/cm}^2$  very strong optical saturation occurs whatever the laser FWHM and operation regime (absorption rates well below 1%).

The observed modification of absorption profiles and atomic resonance line saturation rates is evidence of a strong variation of the spectral coverage between the Doppler and laser profiles under the influence of the operating conditions of the loop mirror cavity. The absorption measurements do not provide as many details on the mode structure and behavior of the fiber laser as do the optical spectral measurements in section 3. But they are rather easy to carry out, and the experimental data can be quantitatively analyzed to get a relevant characterization of the laser features for OP purposes.

To emphasize the influence of the laser spectral characteristics on the response of the atomic system, Fig. 11 displays the change of absorption rates with the laser FWHM for various light power densities shined onto the gas sample. Fig. 11a shows the expected crossover behav-

ing discussed in section 2. The location of the absorption maximum moves towards  $L/D \geq 1$  as the laser power increases as indicated by the computations. At very high powers absorption stops varying with the laser FWHM for  $L/D > 1$ . Relevant experimental data with  $L/D < 1$  are not available with the loop mirror oscillator. The results obtained outside the multimode regime (appearing at  $L/D < 0.56$  in Fig. 11b) have been included only to visualize the amplitude of absorption changes observed at small  $P_{\text{pump}}$ . But, as demonstrated in the previous section, the measured FWHMs (1-1.1 GHz below  $P_{\text{pump}} < 920 \text{ mW}$ ) indeed result from frequency jitter and on their time scale the atoms actually interact with a finite set of discrete modes. This situation might tentatively be described by a set narrow continuous distributions with increasing effective FWHMs (to account for the observed change in IN spectra envelopes with  $P_{\text{pump}}$ ). This would certainly make the low  $P_{\text{pump}}$  data delineate clear absorption maxima in Fig. 11b, with location and rounded shape closer to expectations. However the values of these effective FWHMs are difficult to accurately assess a priori, and their meaning and relevance for further studies are questionable considering the crude description of interaction probabilities between atoms and photons in the model.

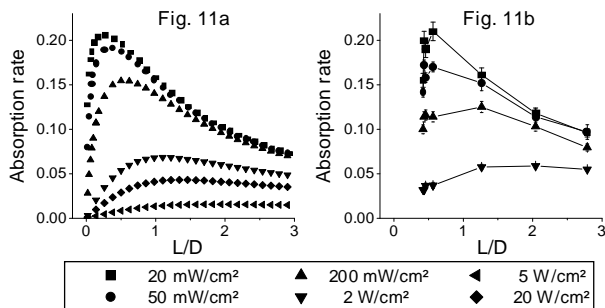


**Fig. 11** Absorption versus laser FWHM  $L$  (scaled to the Doppler width  $D$ ), for various light power densities. Fig. 11a: Computed results using the phenomenological OP model [10]. Fig. 11b: Experimental measurements with the loop mirror oscillator (data sets extracted from Fig. 10).

ior between the high and low power limits qualitatively discussed above. These results are obtained with the phenomenological OP model described in [10], using for the spectral coverage parameter  $X_s$  the rough estimate  $\text{erf}(\sqrt{\ln(2)}L/D)$  introduced in section 2. The experimental data are plotted in Fig. 11b. Measurements appear to be in good qualitative agreement with the computed estimates. For  $P_{\text{pump}} > 920 \text{ mW}$  (data points with  $L/D \geq 1$  in Fig. 11b) we observe at the lowest power densities the expected strong absorption decrease with laser FWHM, above a maximum located somewhere below  $L/D = 0.5$ . The dominant contribution here comes from the growing fraction of off resonance photons in the incident beam, resulting in the  $1/\sqrt{1 + L^2/D^2}$  scal-

#### 4.3 Laser optimization for OP applications

Data in Fig. 10 and 11 indicate that in order to optimize absorption the laser FWHM should lie somewhere between 1 and 2.4 GHz, depending on laser intensity. For OP purposes the laser intensities are usually on the order of  $1 \text{ W/cm}^2$ . Therefore the optimal emission bandwidth should indeed be comparable to the atomic Doppler line width, as qualitatively expected from the discussion in section 2. However this FWHM range cannot be properly investigated with the loop mirror cavity oscillator, due to the abrupt FWHM jump from 1.1 to 2.5 GHz (see Fig. 8) as well as the switching from quasi-singlemode to truly multimode operation. The cavity configuration needs to be changed to achieve multimode operation and laser FWHM adjustable down to 1 GHz.

This is achieved with double FBG linear cavities, using a high reflectivity fiber Bragg grating instead of the loop mirror. The architecture of the double FBR oscillator is depicted in Fig. 12 (master oscillator). With that cavity configuration the threshold for the instability onset is more easily reduced since FBG mirrors have no intrinsic losses.

Optimization of the FBG characteristics turns out to be crucial to obtain both stable multimode operation and narrow spectral bandwidth [30, 31]. The selective low reflectivity FBG mainly determines the smallest FWHM achievable in multimode operation ( $\sim 1 \text{ GHz}$ ). Most frequently the range of launched pump powers where the double FBG oscillators exhibit unstable behavior is very

small. Sometimes no self-pulsing is observed, even close to laser threshold. The FWHM of the double FBG oscillator increases with the pump power. It can thus be adjusted to optimize the OP performances of the laser. However the pump power also directly controls the power delivered by the oscillator. Therefore, to use it as a master oscillator, care must be taken to get enough output power to feed into the high gain power fiber amplifier. Recently considerable progress has been made in the processes used to imprint Bragg grating patterns onto photosensitive fibers. Quality FBG tailored to the user's specifications are now available. This, combined with a better control of all loss sources inside the laser cavity (e.g. in the fiber splicings), allows to routinely build multimode tunable fiber oscillators with adjustable FWHM between 1 and 2 GHz.

Fig. 12 shows the complete structure of the dedicated all-fiber MOPFA lasers designed for operation at 1083 nm with optimized spectral characteristics in view of OP applications. The power booster is here for instance a 5W fiber power amplifier with two-stage architecture. Linear polarization is required at the output fiber connector. For the user's convenience the output fiber may be a few meters long. Polarization maintaining fibers are available but still quite expensive. A mechanical polarization controller is thus included in the laser to pre-compensate for polarization changes induced by light propagation in the output fiber.

Test measurements are performed in helium cells with a double FBG oscillator in MOPFA configuration with a single-stage 2W fiber amplifier, and two other ones with 5W fiber amplifiers. These lasers achieve broadband multimode emission respectively with 1.63, 1.67 and 2.10 GHz FWHMs (measured at the He resonance wavelength).

Fig. 13 displays absorption data for the 1.63 GHz FWHM fiber laser with double FBG cavity. Comparison is made with concomitant measurements performed in fully identical conditions with a singlemode laser diode. We use here the same 1.6 mbar  $^3\text{He}$  cell as that used to test the loop mirror oscillator (Fig. 10 and 11). However for the present series of measurements the discharge is stronger, leading to more metastable atoms excited in the gas and proportionally higher absorption rates.

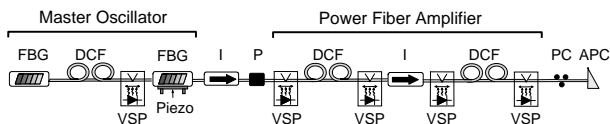


**Fig. 12** All-fiber 1083 nm MOPFA laser optimized for MEOP applications. The dedicated fiber oscillator with double FBG linear cavity is attached to a two-stage Yb-doped DCF power amplifier. VSP: V-groove side pumping; I: optical isolator; P: polarizer; PC: polarization controller; APC: angle polished connector.

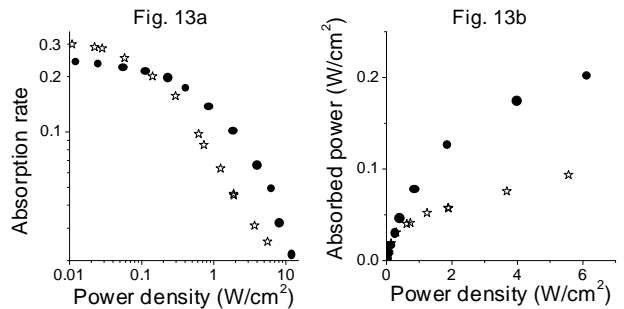


**Fig. 13** Absorption rates (Fig. 13a) and deposited light power density (Fig. 13b) in the 1.6 mbar  $^3\text{He}$  cell, measured in identical conditions for a 1.64 GHz FWHM double FBG oscillator (solid dots) and a DBR laser diode (open stars) tuned to the  $C_9$  line.

Fig. 13a shows that at the limit of very low power densities (no optical saturation) the absorption rate of the fiber laser is  $0.77 \pm 0.02$  times that of the DBR diode. This is in very good agreement with the expected decrease obtained from the convolution of the laser and atomic line profiles ( $1/\sqrt{1+L^2/D^2} = 0.772$  for a laser FWHM  $L = 1.63$  GHz). Saturation occurs at high powers, but clearly in a much less severe manner for the multimode laser than for the singlemode one. The measured threshold power density  $\mathcal{P}_{1/3}$  is much larger for the fiber laser ( $3.1 \text{ W/cm}^2$ ) than for the DBR diode ( $0.6 \text{ W/cm}^2$ ). As a consequence the absorbed light power can be as much as twice larger for the broadband fiber laser at high power densities (Fig. 13b).

Another set of comparative measurements is performed with the two double FBG cavity oscillators in 5W MOPFA configuration that have 1.67 and 2.10 GHz FWHMs (Fig. 14). The absorption rate measured at very low power densi-

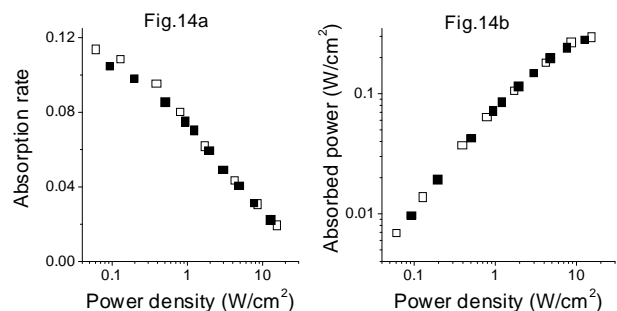


**Fig. 14** Comparison of absorption measurements performed with 1.7 (solid squares) and 2.1 GHz (open squares) FWHM multimode fiber lasers involving double FBG cavity oscillators; 1.6 mbar  $^3\text{He}$  cell,  $C_9$  light with linear polarization.

ties is 7% larger for the 1.67 GHz broad laser than for the 2.10 GHz one (Fig. 14a). This can be explained by a smaller bandwidth being there more favorable in the  $L/D \approx 1$  range due to the  $1/\sqrt{1+L^2/D^2}$  scaling. It

is also in good agreement with both FWHMs exceeding the best value for maximum absorption at low power densities as suggested by the loop mirror oscillator tests and confirmed by the numerical calculations ( $L = 0.6$ – $1$  GHz, see Fig. 11). No significant difference between the two multimode lasers is observed above  $1 \text{ W/cm}^2$ . This again matches the weak FWHM dependence of the test results and expectations at high power densities (see Fig. 11). Saturation effects strongly increase above  $1 \text{ W/cm}^2$  (Fig. 14a), limiting the rise of deposited power with incident laser power at higher photon flux densities (Fig. 14b).

The typical OP power densities presently used for production of polarized gas lie between  $0.2$  and  $2.4 \text{ W/cm}^2$  [11, 12, 23, 42, 43]. Our results suggest that optimal performances should be achieved with  $2$  GHz-broad lasers at the upper end of that power range, while  $1.2$ – $1.5$  GHz FWHMs might be preferred at the lower end. Preliminary OP measurements performed around  $1 \text{ W/cm}^2$  indicate that the nuclear polarizations obtained in a  $1.3$  mbar  $^3\text{He}$  cell at moderate discharge intensity are  $10\%$  higher for the  $1.67$  GHz FWHM laser than for the  $2.10$  GHz FWHM one. Further experimental work is still needed to reliably assess the optimal line width in multimode operation with respect to the OP performances in well controlled situations. For this purpose the double FBG cavity configuration provides the most convenient opportunity to vary the laser FWHM ad libitum, from one to a few GHz, through the control of the launched pump power. Systematic measurements are in progress, both in sealed cells and in the presence of gas flow. However, due the variety of OP conditions to be explored, efforts to develop a predictive model based on accurate phenomenological input parameters must be also continued to provide a comprehensive overview of the expected optimal OP performances.

## 5 Conclusion

We have demonstrated and tested the operation of all-fiber tunable lasers at  $1083 \text{ nm}$  for  $^3\text{He}$  OP applications. In the linear cavity configuration, with a loop mirror and a low reflectivity fiber Bragg grating, evolution of the laser line width and mode structure with launched pump power has been observed and analyzed in detail using a variety of optical measurements. In view of OP applications, simple tests have also been presented to characterize the laser at the He wavelength on the relevant time scales. The need for a multimode light source with a FWHM matched to the atomic line width is clearly identified. It is met with the double FBG cavity fiber oscillators.

These stable multimode oscillators with  $1$ – $2$  GHz spectral FWHM are now combined with power amplifiers in commercially available MOPFA devices, providing stand-alone all-fiber laser sources delivering up to  $10 \text{ W}$  output

power [31]. Compact turn-key  $1083 \text{ nm}$  lasers that require no servicing from the user are attractive and convenient tools for research work. They are also ideally suited for operation outside the physics laboratories, e.g. at the clinics for on-site production of hyperpolarized gas next to the magnetic resonance imaging scanner [42]. In a higher stage MOPFA configuration, a  $1$  or  $2 \text{ W}$  all-fiber MOPFA laser with double FBG oscillator can be used as a master laser to launch a more powerful fiber power booster in order to take full advantage of the truly multimode structure and allow very large scale production of highly polarized  $^3\text{He}$  gas. Preliminary tests of operation at  $1083 \text{ nm}$  up to  $40 \text{ W}$  have been performed [44].

For the users, precise line width specifications and identification of the ultimate physical limitations of MEOP will contribute to bring new record  $^3\text{He}$  nuclear polarizations within reach. For the laser manufacturers, the main technical challenge now lies in the cost-effective production of robust, reliable and very powerful fiber sources for production of large quantities of polarized gas to support the wide dissemination of established applications of hyperpolarized  $^3\text{He}$  gas and the emergence of new ones [45, 46, 47, 48, 49, 50, 51, 52, 53, 54, 55].

## References

1. M. Leduc, *J. Phys. Colloque* **51**, C6-317 (1990).
2. J. Becker *et al.*, *Nuc. Instr. & Meth. A* **402**, 327 (1998).
3. D. Rohe *et al.*, *Phys. Rev. Lett.* **83**, 4257 (1999).
4. G.L. Jones *et al.*, *Nuc. Instr. & Meth. A* **440**, 772 (2000).
5. G. Tastevin, *Physica Scripta* **T86**, 46 (2000).
6. T. Chupp and S. Swanson, *Adv. At. Mol. Opt. Phys.* **45**, 51 (2001).
7. H.-U. Kauczor, X.J. Chen, E.J.R. van Beek and W.G. Schreiber, *Eur. Resp. J.* **17**, 1 (2001).
8. F.D. Colegrove, L.D. Schearer and G.K. Walters, *Phys. Rev.* **132**, 2561 (1963).
9. P.-J. Nacher and M. Leduc, *J. Phys. Paris* **46**, 2057 (1985).
10. M. Leduc, P.-J. Nacher, G. Tastevin and E. Courtade, *Hyperfine Interactions* **127**, 443 (2000).
11. J. Becker *et al.*, *Nucl. Instr. and Meth. A* **346**, 45 (1994).
12. P.-J. Nacher, G. Tastevin, X. Maitre, X. Dollat, B. Lemaire and J. Olejnik, *Eur. Radiol.* **9**, B18 (1999).
13. T. R. Gentile *et al.*, *Magn. Reson. Med.* **43**, 290 (2000).
14. C.G. Aminoff, C. Larat, M. Leduc and F. Laloë, *Revue. Phys. Appl.* **24**, 827 (1989).
15. E. Stoltz, M. Meyerhoff, N. Bigelow, M. Leduc, P.-J. Nacher and G. Tastevin, *Appl. Phys.* **B63**, 629 (1996).
16. S.V. Chernikov, J.R. Taylor, N.S. Platonov, V.P. Gaponstev, P.-J. Nacher, G. Tastevin, M. Leduc and M.J. Barlow, *Electronics Lett.* **33**, 787 (1997).
17. R. M. Mueller, *Physica B* **297**, 277 (2001).
18. E. Courtade, F. Marion, P.-J. Nacher, G. Tastevin, K. Kiersnowski and T. Dohnalik, *Eur. Phys. J. D* **21**, 25 (2002).
19. E. Courtade, F. Marion, P.J. Nacher, G. Tastevin, T. Dohnalik and K. Kiersnowski, *Hyperfine Interactions* **127**, 451 (2000).

20. P.J. Nacher, E. Courtade, M. Abboud, A. Sinatra and G. Tastevin, *Acta Physica Polonica* **33**, 2225 (2002).
21. M. Pinard and J. van der Linde, *Can. J. Phys.* **52**, 1615 (1974).
22. F. Emmert, H.H. Angermann, R. Dux and H. Langhoff, *J. Phys. D: Appl. Phys.* **21**, 667 (1988).
23. T.R. Gentile, D.R. Rich, A.K. Thompson, W.M. Snow, G.L. Jones, *J. Res. Natl. Inst. Stand. Technol.* **106**, 709 (2001).
24. E. Courtade, PhD Thesis, Paris (2001); *unpublished, in French; available at <http://tel.ccsd.cnrs.fr/>*.
25. T.R. Gentile, M. Hayden, M. Barlow, *submitted for publication*.
26. J.S. Major, D.F. Welch, *Electron. Lett.* **29**, 2121 (1993).
27. J.M. Daniels, L.D. Scheerer, M. Leduc and P.-J. Nacher, *J. Opt. Soc. Am. B* **4**, 1133 (1987).
28. T.R. Gentile and R.D. McKeweown, *Phys. Rev. A* **47**, 456 (1993).
29. M. Auerbach, D. Wandt, C. Fallnich, H. Welling, S. Unger, *Optics Communications* **195**, 437 (2001).
30. S. Bordais, PhD Thesis, Rennes (2002); *unpublished, in French; available at <http://tel.ccsd.cnrs.fr/>*.
31. S. Bordais, S. Grot, Y. Jaouen, P. Besnard and M. Le Flohic, *to appear in Applied Optics (2003)*.
32. H. M. Pask, R. J. Carman, D. C. Hanna, A. C. Tropper, C. J. Mackechnie, P. R. Barber and J. M. Dawes, *IEEE J. of Selected Topics in Quant. Electron.* **1**, 2 (1995).
33. V. Dominic, S. MacCormack, R. Waarts, S. Sanders, S. Bicknese, R. Dohle, E. Wolak, P.S. Yeh and E. Zucker, *Electron. Lett.* **35**, 1158 (1999).
34. D. J. Ripin, L. Goldberg, *Elect. Lett.* **31**, 2204 (1995).
35. D.B. Mortimore, *J. Lightwave Technol.* **6**, 1217 (1988).
36. S. V. Chernikov, Y. Zhu, J. R. Taylor, V. P. Gapontsev, *Optics Letters Vol.* **22**, 298 (1997).
37. A. Hideur, T. Chartier, C. Özkul, F. Sanchez, *Opt. Commun.* **186**, 311 (2000).
38. M. Auerbach, P. Adel, D. Wandt, C. Fallnich, S. Unger, S. Jetschke, H.-R. Mueller, *Optics Express* **10**, 139 (2002).
39. E. Lacot, F. Stoeckel and M. Chenevriev, *Phys. Rev. A* **49**, 3997 (1994).
40. F. Sanchez, P. Le Boudec, P.-L. François and G. Stephan, *Phys. Rev. A* **48**, 2220 (1993).
41. B. Ortac, A. Hideur, T. Chartier, M. Brunel, G. Martel, M. Sahli and F. Sanchez, *Optics Communications* **215**, 389 (2003).
42. J. Choukeife, X. Maitre, G. Tastevin and P.-J. Nacher, *Proc. Intl Soc. Mag. Reson. Med.* **11**, 1391 (2003).
43. J. Schmideskamp, A. Deninger, M. Ebert, W. Heil, S. Hiebel, E.W. Otten, R. Surkau, D. Rudersdorf, M. Wolf and T. Grosmann, *Proc. Intl Soc. Mag. Reson. Med.* **11**, 1392 (2003).
44. W. Heil, *private communication*.
45. H.U. Kauczor, A. Hanke and E.J.R. van Beek, *Eur. Rad.* **12**, 1962 (2002).
46. H.E. Moller, X.J. Chen, B. Saam, K.D. Hagspiel, A.G. Johnson, A.T. Altes, E.E. deLange and H.U. Kauczor, *Magn. Reson. Med.* **47**, 1209 (2002).
47. C.B. Bidinosti, J. Choukeife, P.-J. Nacher and G. Tastevin, *J. Magn. Reson.* **162**, 122 (2003).
48. W.C. Chen et al, *Physica B-Cond. Mat.* **335**, 196 (2003).
49. W. Heil, K.H. Andersen, R. Cywinski, H. Humblot, C. Ritter, T.W. Roberts and J.R. Stewart, *Nucl. Instrum. Meth. A* **551**, 485 (2002).
50. F. Radu, A. Vorobiev, J. Major, H. Humblot, K. Westerholt and H. Zabel, *Physica B-Cond. Mat.* **335**, 63 (2003).
51. W. Korsch, pp. 249-55 in *Testing QCD Through Spin Observables in Nuclear Targets* (Editors: D.G. Crabb, D.B. Day and J.P. Chen, World Scientific, Singapore 2003).
52. G. Tastevin, P.-J. Nacher and J. Choukeife, *Physica B* **329-333**, 303 (2003).
53. P.-J. Nacher, N. Piegay, F. Marion F. and G. Tastevin, *J. Low Temp. Phys.* **126**, 145 (2002).
54. Y. Borisov, Heil W, M. Leduc, V. Lobashev, E.W. Otten and Y. Sobolev, *Nucl. Instrum. Meth. A* **440**, 483 (2000).
55. S.J. Zweben, T.W. Kornack, D. Majeski, G. Scilling, C.H. Skinner; R. Wilson and N. Kuzma, *Rev. Sci. Instrum.* **74**, 1460 (2003).